Monthly Notices
of the
ROYAL ASTRONOMICAL SOCIETY

MNRAS **491,** 1043–1056 (2020)
Advance Access publication 2019 October 31

doi:10.1093/mnras/stz3065

Magnetohydrodynamical origin of eclipsing time variations in post-common-envelope binaries for solar mass secondaries

Felipe H. Navarrete,[1]★ Dominik R. G. Schleicher,[1] Petri J. Käpylä,[2,3] Jennifer Schober,[4] Marcel Völschow[5] and Ronald E. Mennickent[1]

[1]*Departamento de Astronomía, Facultad Ciencias Físicas y Matemáticas, Universidad de Concepción, Av. Esteban Iturra s/n Barrio Universitario, Casilla 160-C, 4070386 Concepción, Chile*
[2]*Fakultät für Physik, Georg-August-Universität Göttingen, Friedrich-Hund-Platz 1, D-37077 Göttingen, Germany*
[3]*ReSoLVE Centre of Excellence, Department of Computer Science, Aalto University, PO Box 15400, FI-00076 Aalto, Finland*
[4]*Laboratoire d'astrophysique, Observatoire de Sauverny, CH-1290 Versoix, Switzerland*
[5]*Hamburg Observatory, Hamburg University, Gojenbergsweg 112, D-21029 Hamburg, Germany*

Accepted 2019 October 28. Received 2019 October 3; in original form 2019 June 17

ABSTRACT

Eclipsing time variations have been observed for a wide range of binary systems, including post-common-envelope binaries. A frequently proposed explanation, apart from the possibility of having a third body, is the effect of magnetic activity, which may alter the internal structure of the secondary star, particularly its quadrupole moment, and thereby cause quasi-periodic oscillations. Here, we present two compressible non-ideal magnetohydrodynamical simulations of the magnetic dynamo in a solar mass star, one of them with three times the solar rotation rate ('slow rotator'), and the other one with 20 times the solar rotation rate ('rapid rotator'), to account for the high rotational velocities in close binary systems. For the slow rotator, we find that both the magnetic field and the stellar quadrupole moment change in a quasi-periodic manner, leading to $O - C$ (observed minus corrected times of the eclipse) variations of $\sim$0.025 s. For the rapid rotator, the behaviour of the magnetic field as well as the quadrupole moment changes becomes considerably more complex, due to the less coherent dynamo solution. The resulting $O - C$ variations are of the order of 0.13 s. The observed system V471 Tau shows two modes of eclipsing time variations, with amplitudes of 151 and 20 s, respectively. However, the current simulations may not capture all relevant effects due to the neglect of the centrifugal force and self-gravity. Considering the model limitations and that the rotation of V471 Tau is still a factor of 2.5 faster than our rapid rotator, it may be conceivable to reach the observed magnitudes.

Key words: dynamo – MHD – methods: numerical – binaries: eclipsing – stars: rotation.

1 INTRODUCTION

Post-common-envelope binaries (PCEBs) are close binaries that consist of a low-mass main-sequence star and a white dwarf (WD). Such systems are expected to form when the more massive component evolves until its surface extends beyond the outer Lagrangian point and eventually engulfs its companion (Paczynski 1976). Then the less massive star experiences friction and deposits orbital energy and angular momentum into the common envelope (CE). It spirals inwards until the envelope is expelled due to the energy transfer, leaving a close binary, typically consisting of an M dwarf (dM) or a subdwarf and a WD (see e.g. Parsons et al. 2013). The CE model has been revised and extended by various authors, including Meyer & Meyer-Hofmeister (1979), Iben & Livio (1993), Taam & Sandquist (2000), Webbink (2008), and Taam & Ricker (2010).

For about 90 per cent of these systems, eclipsing time variations have been observed (e.g. Zorotovic & Schreiber 2013; Bours et al. 2016). The variations occur on rather long time-scales of the order of 20 yr or more. Two possible interpretations of these variations are commonly discussed in the literature: the first is the presence of a third body, i.e. a planet or a brown dwarf, which would cause apparent eclipsing time variations due to the light-traveltime (LTT) effect, i.e. the change in the light traveltime to the observer due to the change of distance as the PCEB rotates around the common centre of mass (e.g. Beuermann et al. 2010; Beuermann, Dreizler & Hessman 2013). Clearly, this effect requires rather massive planets ($>M_{\rm J}$, where $M_{\rm J}$ is the mass of Jupiter) on extended orbits ($>$au) to produce significant variations. Alternatively, such variations may also be produced through the Applegate

★ E-mail: felnavarrete@udec.cl

mechanism (Applegate 1992), which will be described in further detail below.

If the LTT is adopted, the eclipsing time variations imply the presence of two planets with masses of 5.6 and 2.1 M_J and semimajor axis of 5 and 3.4 au, respectively, in the system NN Ser (Beuermann et al. 2010, 2013), which often serves as a reference system for typical PCEBs. Beuermann et al. (2013) demonstrated the dynamical stability of these orbits, which was independently confirmed by Horner et al. (2012). However, when the additional data by Bours et al. (2016) are considered, they require an extra quadratic term in the expression for the eclipsing times if they want to maintain the planet solution. The physical origin of such an additional term is, however, unclear. In case of the system HW Vir, a two-planet solution appears to be secularly stable (Beuermann et al. 2012). A final conclusion on the stability of orbits in Hu Aqr is still pending (Goździewski et al. 2012; Hinse et al. 2012; Bours et al. 2014; Goździewski et al. 2015), and similarly for QS Vir (Parsons et al. 2010b). In the case of the system V471 Tau, the proposed third body has been searched via direct imaging, but has not been found (Hardy et al. 2015). Using the orbital period of the system (12.5 h) and the spin period (9.25 min) of the WD as two independent clocks, Vanderbosch et al. (2017) have concluded that a third body interpretation cannot adequately explain the nature of this system.

If the planets in NN Ser are real, they should also be dynamically young, as the WD has an age of only 10^6 yr (Parsons et al. 2010a). While their existence is highly speculative, they have at least two possible origins. The so-called first-generation scenario proposes that they formed together with the binary and then survived the CE phase, while the second-generation scenario implies that they formed through the material ejected during the CE phase. A hybrid scenario may be also possible, with accretion of the ejected gas on to already existing planets. Several studies have been carried out on this matter (e.g. Bear & Soker 2014; Schleicher & Dreizler 2014; Völschow, Banerjee & Hessman 2014), though it is currently difficult to draw any final conclusions.

The other possible explanation of the eclipsing time variations is magnetic activity. Historically, in particular the Applegate mechanism (Applegate 1992) has been a relevant scenario, in which the magnetic activity of the secondary stars leads to a redistribution of the stellar angular momentum, thus changing its gravitational quadrupole moment. This in turn produces a variation of the binary separation. The original Applegate model has been improved by several authors. For instance, Lanza & Rodonò (1999) improved the model by adopting a consistent description of stellar virial equilibrium. Brinkworth et al. (2006) extended the model introducing a finite shell formalism, considering the exchange of the angular momentum between the shell and the core. Völschow et al. (2016) examined their model in more detail and applied it to a sample of 16 close binary systems (predominantly PCEBs), showing that the Applegate mechanism is a viable process in the shortest and most massive binary systems. The corresponding model has been made public through the Applegate calculator,[1] and shows that the mechanism is favoured in particular for rapidly rotating systems (Navarrete et al. 2018).

In addition to the finite shell model, Lanza & Rodonò (2004) and Lanza (2005) presented a one-dimensional framework based on the angular momentum transport equations, using simplifying assumptions of magnetohydrodynamical (MHD) turbulence and the mean magnetic field. We have extended this framework in Völschow et al. (2018), considering in particular time-dependent hydrodynamic and magnetic fluctuations assuming a magnetic activity cycle, as well as a superposition of different modes. For typical RS Canum Venaticorum (RS CVn) systems, which are detached binaries typically composed of a chromospherically active G or K star, the expected eclipsing time variations are, however, two orders of magnitude lower than observed. The most promising Applegate candidates are PCEBs with secondary masses of $\sim$0.35 $M_\odot$ (Völschow et al. 2018), as these produce more energy through nuclear burning and can thus more easily redistribute angular momentum as required by the Applegate mechanism, while simultaneously not being critically affected by the presence of a radiative core.

The presence of magnetic activity should be expected in these systems due to the convective envelopes of the secondaries and their rapid rotation. A corresponding dynamo model has been put forward by Rüdiger et al. (2002). Observationally, magnetic activity has been inferred on many occasions. In the case of V471 Tau, it has been probed via photometric variability, flaring events, and Hα emission along with a strong X-ray signal (Kamiński et al. 2007; Pandey & Singh 2008). For DP Leo, magnetic activity has been revealed through X-ray observations (Schwope et al. 2002). In the system QS Vir, it is indicated via detections of Ca II emission and Doppler imaging (Ribeiro et al. 2010), as well as observed coronal emission (Matranga et al. 2012). In case of HR 1099, a 40 yr X-ray light curve suggesting a long-term cycle was recently compiled by Perdelwitz et al. (2018), and similar studies have been pursued via optical data (e.g. Donati et al. 2003; Lanza et al. 2006; Berdyugina & Henry 2007; Muneer et al. 2010).

While magnetic activity is potentially relevant to explain the origin of the eclipsing time variations, its effects on the stellar structure so far have only been explored via finite shell or 1D models, in both of which the presence of a dynamo was externally imposed. However, a self-consistent modelling of the dynamo and its interaction with the stellar structure may be crucial, and is only possible within 3D MHD simulations. While stellar dynamo models have previously been pursued (see e.g. Yadav et al. 2016), the latter was done in the anelastic limit, which does not allow to explore the effect of the dynamo on to the stellar structure. Here, as a first step, we will employ a fully compressible set-up developed by Käpylä et al. (2013) for a solar mass star although with rotation rates exceeding the solar one. These models allow the quantification of changes in stellar structure due to the dynamo. While solar mass stars are not very common in post-common-envelope systems, they do occasionally occur, as for instance the secondary of V471 Tau has a mass of $0.93 \pm 0.07\,M_\odot$ (Zorotovic & Schreiber 2013), and is thus still consistent with being a solar mass star. Independently, we of course stress that this is an exploratory study that should be extended to stars of different masses as well.

In Section 2, we will briefly introduce the PENCIL CODE[2] (Brandenburg & Dobler 2002; Brandenburg 2003) as well as the set-up employed here, which is based on previous developments by Käpylä et al. (2013). In these simulations, the Rayleigh number, which describes the ratio of the time-scale for thermal transport via diffusion to the time-scale for thermal transport via convection, is, however, much smaller than in reality due to the higher diffusivities required for numerical stability; see detailed discussions in Käpylä et al. (2013) and Kupka & Muthsam (2017). Another caveat of fully

[1] Applegate calculator: http://theorygroup-concepcion.cl/applegate/index.php

[2] https://github.com/pencil-code/

compressible simulations of solar-like stars is that the low Mach number in the deep parts of the convection zone (CZ) necessitates a very short time-step and that the thermal relaxation occurs in the Kelvin–Helmholtz time-scale that is of the order of 10^7 (10^5) yr for the whole Sun (solar CZ) (see e.g. Kupka & Muthsam 2017). Thus, to bring the dynamic and acoustic time-scales closer to each other and to shorten the Kelvin–Helmholtz time-scale, the energy flux needs to be enhanced (see also Brandenburg et al. 2005). To compensate for this and to obtain a comparable rotational influence on the flow as in real stars, which is the key factor determining their dynamo properties, the angular velocity needs to be increased proportional to one-third power of the increase of the energy flux (see a detailed description in Käpylä et al. 2019). For this reason, the effect of the centrifugal force has been omitted in this formulation of the Navier–Stokes equation, as the resulting centrifugal force would be too high, thereby significantly altering the hydrostatic balance (Käpylä et al. 2011, 2013). With this in mind, we note that our simulations present only a first step, where the redistribution of material can be explored for instance due to meridional flows, and we will not probe the effect originally proposed by Applegate (1992). Nevertheless, the occurrence of quadrupole moment variations even in the absence of the centrifugal force term is a central outcome of the simulations. The results of our simulations are presented in Section 3, including a hydrodynamical reference run and two MHD simulations. Our discussion and conclusions are presented in Section 4.

2 METHODS

2.1 PENCIL CODE

The PENCIL CODE (Brandenburg & Dobler 2002; Brandenburg 2003) is a finite-difference code written in FORTRAN 95. It uses sixth-order spatial derivatives and a third-order Runge–Kutta time integrator scheme, which makes the code particularly useful for studying weakly compressible turbulent flows. For the time-stepping, a high-order scheme is implemented in order to reduce amplitude errors and to allow longer time-steps, which is the *RK-2N* Runge–Kutta scheme (Williamson 1980), where the '2N' stands for its memory consumption of two chunks. The time-step is specified by the Courant time-step. The *Message Passing Interface* (MPI) is used for parallelization.

2.2 The model

The model we use here is based on those used by Cole et al. (2014) and Viviani et al. (2018) and is described here for completeness. The computational domain is spherical but without the poles, which allows to reach a higher spatial resolution but at the cost of omitting connecting flows across the poles and introducing artificial boundaries at high latitudes. The domain (r, θ, ϕ) denotes radial, colatitudinal, and longitudinal directions. The radius extends from 0.7 $R_\odot$ (the bottom of the CZ) to 1.0 $R_\odot$, where $R_\odot$ is the solar radius; θ goes from $\pi/12$ to $11\pi/12$, and ϕ from 0 to 2π. The corresponding grid resolution is $128 \times 256 \times 512$. We employ the compressible non-ideal MHD equations in the following form:

$$\frac{\partial \boldsymbol{A}}{\partial t} = \boldsymbol{u} \times \boldsymbol{B} - \mu_0 \eta \boldsymbol{J}, \tag{1}$$

$$\frac{\mathrm{D} \ln \rho}{\mathrm{D}t} = -\boldsymbol{\nabla} \cdot \boldsymbol{u}, \tag{2}$$

$$\frac{\mathrm{D}\boldsymbol{u}}{\mathrm{D}t} = \boldsymbol{g} - 2\boldsymbol{\Omega}_0 \times \boldsymbol{u} + \tfrac{1}{\rho}(\boldsymbol{J} \times \boldsymbol{B} - \boldsymbol{\nabla} p + \boldsymbol{\nabla} \cdot 2\nu\rho\mathbf{S}), \tag{3}$$

$$T\frac{\mathrm{D}s}{\mathrm{D}t} = \tfrac{1}{\rho}\left\{-\boldsymbol{\nabla} \cdot \left(\boldsymbol{F}^{\mathrm{rad}} + \boldsymbol{F}^{\mathrm{SGS}}\right) + \mu_0 \eta \boldsymbol{J}^2\right\} + 2\nu\mathbf{S}^2, \tag{4}$$

where $\boldsymbol{A}$ is the magnetic vector potential, $\boldsymbol{u}$ and $\boldsymbol{B} = \boldsymbol{\nabla} \times \boldsymbol{A}$ are the velocity and magnetic field, $\boldsymbol{J} = \mu_0^{-1} \boldsymbol{\nabla} \times \boldsymbol{B}$ is the electric current density with μ_0 being the vacuum permeability. $\mathrm{D}/\mathrm{D}t = \partial/\partial t + \boldsymbol{u} \cdot \boldsymbol{\nabla}$ is the convective derivative, ρ is the density, and

$$\boldsymbol{F}^{\mathrm{rad}} = -K \boldsymbol{\nabla} T, \tag{5}$$

and

$$\boldsymbol{F}^{\mathrm{SGS}} = -\chi_{\mathrm{SGS}} \rho T \boldsymbol{\nabla} s, \tag{6}$$

are the radiative and subgrid scale (SGS) fluxes. The former accounts for the flux coming from the radiative core and the latter is added to stabilize the scheme and to account for the unresolved turbulent transport of heat. K and χ_{SGS} are the radiative heat conductivity and turbulent entropy diffusivity, respectively. s is the specific entropy, p is the pressure, and T is temperature. Furthermore, the system of equations (1)–(4) is closed by assuming an ideal gas law,

$$p = (\gamma - 1)\rho e, \tag{7}$$

where $\gamma = c_{\mathrm{P}}/c_{\mathrm{V}} = 5/3$ is the ratio of specific heats at constant pressure and volume, and $e = c_{\mathrm{V}} T$ is the specific internal energy. $\mathbf{S}$ is the traceless rate-of-strain tensor

$$\mathsf{S}_{ij} = \frac{1}{2}(u_{i;j} + u_{j;i}) - \frac{1}{3}\delta_{ij} \boldsymbol{\nabla} \cdot \boldsymbol{u}, \tag{8}$$

where semicolons denote covariant differentiation. $\boldsymbol{g} = -GM\hat{\boldsymbol{r}}/r^2$ is the gravitational acceleration with G being the gravitational constant, M the stellar mass, and $\hat{\boldsymbol{r}}$ the radial unit vector. The stellar rotation vector is given as $\Omega_0 = (\cos\theta, -\sin\theta, 0)\Omega_0$. As already discussed in the introduction, the formulation of the Navier–Stokes equation employed here does not include the centrifugal force term, which would be unrealistically high (see Käpylä et al. 2011, 2013, 2019, for details).

2.3 Initial and boundary conditions

The initial state is entropic with a temperature gradient given as

$$\frac{\partial T}{\partial r} = -\frac{GM/r^2}{c_{\mathrm{V}}(\gamma - 1)(n_{\mathrm{ad}} + 1)}, \tag{9}$$

where $n_{\mathrm{ad}} = 3/2$ is the polytropic index for adiabatic stratification. The fixed values that define a simulation are (i) the energy flux at the bottom,

$$F_b = -K \left(\frac{\partial T}{\partial r}\right)\Big|_{r=r_0}, \tag{10}$$

where $K = (n + 1)K_0$ is the radiative conductivity, K_0 is a constant (Käpylä et al. 2013), and

$$n = 2.5\left(\frac{r}{r_0}\right)^{-15} - 1. \tag{11}$$

Here $n = n_{\mathrm{ad}}$ at the bottom and $n \to -1$ at the surface. This choice is made to ensure that the radiative flux at the bottom is solely responsible for supplying energy into the system and that convection transport essentially the total flux in the bulk of the CZ. The remaining parameters of the model are (ii) the angular velocity Ω_0, (iii) viscosity ν, (iv) magnetic diffusivity η, and (v) turbulent

heat conductivity $\chi_{\rm SGS}$ and its radial profile (see Käpylä et al. 2013). The turbulent velocity and magnetic fields are initialized with small-scale low-amplitude Gaussian noise perturbations.

2.3.1 Radial boundary

The radial boundaries are assumed to be impenetrable and stress-free, i.e. at $r = r_0,\ R$:

$$u_r = 0, \tag{12}$$

$$\frac{\partial u_\theta}{\partial r} = \frac{u_\theta}{r}, \tag{13}$$

$$\frac{\partial u_\phi}{\partial r} = \frac{u_\phi}{r}. \tag{14}$$

The bottom ($r = r_0 = 0.7R$) is assumed to be a perfect conductor with

$$\frac{\partial A_r}{\partial r} = A_\theta = A_\phi = 0, \tag{15}$$

and at the top ($r = R$) the magnetic field is radial

$$A_r = 0, \tag{16}$$

$$\frac{\partial A_\theta}{\partial r} = -\frac{A_\theta}{r}, \tag{17}$$

$$\frac{\partial A_\phi}{\partial r} = -\frac{A_\phi}{r}. \tag{18}$$

The value of $\partial T/\partial r$ is fixed at the bottom and the upper radial boundary uses a blackbody condition

$$\sigma T^4 = -K\nabla_r T - \chi_{\rm SGS}\rho T\nabla_r s, \tag{19}$$

where σ is a modified value of the Stefan–Bolzmann constant (see Käpylä et al. 2013).

2.3.2 Latitudinal boundary

The latitudinal boundary is also assumed to be stress-free at $\theta = 15^\circ, 165^\circ$

$$\frac{\partial u_r}{\partial \theta} = u_\theta = 0, \tag{20}$$

$$\frac{\partial u_\phi}{\partial \theta} = u_\phi \cot\theta, \tag{21}$$

and a perfect conductor

$$A_r = \frac{\partial A_\theta}{\partial \theta} = A_\phi = 0. \tag{22}$$

Density and entropy are assumed to have zero first derivative on both boundaries, thus suppressing heat fluxes through them.

2.4 Quadrupole moment and its scaling

The quadrupole tensor is defined as

$$Q_{ij} = I_{ij} - \frac{1}{3}\delta_{ij}{\rm Tr}\, I, \tag{23}$$

where Tr denotes the trace and I_{ij} is the tensor of inertia

$$I_{ij} = \int x_i x_j {\rm d}m = \int \rho(\boldsymbol{x}) x_i x_j {\rm d}^3x, \tag{24}$$

where x_i refer to Cartesian coordinates.

As already mentioned in the introduction, the stellar luminosity is enhanced due to numerical constraints (see Brandenburg et al. 2005; Käpylä et al. 2019). As a result, the energy flux coming from the bottom is much higher than in the Sun. The ratio of fluxes $\mathfrak{F}_r$ in the present case is

$$\mathfrak{F}_r = \frac{\mathfrak{F}_{\rm simulation}}{\mathfrak{F}_\odot} = 8.07\times10^5. \tag{25}$$

The increased flux implies that the fluctuations of other quantities are correspondingly enhanced. The fluctuation of the pressure can be written as

$$\Delta p = \left(\frac{\partial p}{\partial \rho}\right)_s \Delta\rho \equiv c_{\rm s}^2\Delta\rho, \tag{26}$$

where the subscript s indicates constant entropy and where $c_{\rm s}$ is the sound speed. Furthermore, variations in pressure scale as

$$\Delta p \sim \rho \boldsymbol{u}^2. \tag{27}$$

Equating (26) and (27) we obtain

$$\frac{\Delta\rho}{\rho} \sim \frac{\boldsymbol{u}^2}{c_s^2} = {\rm Ma}^2. \tag{28}$$

Here Ma is the Mach number, which scales as (e.g. Käpylä 2019; Käpylä et al. 2019)

$${\rm Ma} \sim \mathfrak{F}_{\rm r}^{1/3}, \tag{29}$$

and thus,

$$\Delta\rho \sim \mathfrak{F}_r^{2/3}. \tag{30}$$

All of the numbers given in Sections 3.3.4 and 3.4.4 have been rescaled in this fashion, which corresponds to a factor of $(8.07\times10^5)^{-2/3} \approx 1.15\times10^{-4}$, i.e.

$$Q_{xx} = 1.15\cdot10^{-4}Q_{xx,{\rm sim}}, \tag{31}$$

where the subscript 'sim' denotes the estimated quadrupole moment obtained in the simulations.

Furthermore, we define the Taylor, Coriolis, fluid and magnetic Reynolds, and SGS and magnetic Prandtl numbers as

$${\rm Ta} = \left[\frac{2\Omega_0(0.3R)^2}{\nu}\right]^2,\ {\rm Co} = \frac{2\Omega_0}{u_{\rm rms}k_1}, \tag{32}$$

$${\rm Re} = \frac{u_{\rm rms}}{\nu k_1},\ {\rm Re_M} = \frac{u_{\rm rms}}{\eta k_1}, \tag{33}$$

$${\rm Pr_M} = \frac{\nu}{\eta},\ {\rm Pr_{SGS}} = \frac{\nu}{\chi^{\rm m}_{\rm SGS}}, \tag{34}$$

where $u_{\rm urms}$ is the volume-averaged root-mean-square velocity, $k_1 = 2\pi/0.3R$ is an estimate of the wavenumber of the largest eddies, and $\chi^{\rm m}_{\rm SGS}$ is the SGS entropy diffusion at $r = 0.85\ R_\odot$.

3 RESULTS

In this section, we present our main results obtained from the numerical simulations. In Section 3.1, we introduce the notation used throughout the paper and discuss the overall properties of our simulations. We first discuss a pure hydrodynamical reference run in Section 3.2 to demonstrate that the long-term modulation of the quadrupole moment must have an MHD origin. We then present two MHD models, a slow rotator (three times solar rotation, $P_{\rm rot} =$ 9 d) and a fast rotator (20 times solar rotation, $P_{\rm rot} = 1.4$ d) in Sections 3.3 and 3.4. These values were chosen as the rotation rate in PCEBs is considerably enhanced compared to isolated stars, with a rotation period in V471 Tau of about 0.522 d (Zorotovic & Schreiber 2013).

3.1 Notation and general properties

We label the two MHD simulations according to their rotation rates, namely *run3x* for the three times solar rotation, and *run20x* for the 20 times solar rotation rate. Quantities with an overline indicate an average over the azimuthal angle; e.g. $\overline{B}_r$ indicates an average of the r component of B over ϕ and is given by

$$\overline{B}_r(r,\theta) = \frac{\int B_r(r,\theta,\phi)\,\mathrm{d}\phi}{\int \mathrm{d}\phi}. \tag{35}$$

Other averages are presented inside angular brackets with subscripts and superscripts. For example, $\langle \overline{B}_r \rangle_i^k$ indicates an average of $\overline{B}_r$ in regions denoted with i and k. The subscript indicates the depth at which the quantity of interest is taken and the superscript indicates the latitude where the average is further calculated with the following rules:

$$i = \{\mathrm{s}, \mathrm{m}, \mathrm{b}\}, \tag{36}$$

$$k = \{\mathrm{np}, \mathrm{eq}, \mathrm{sp}\}, \tag{37}$$

where

$$\mathrm{s} = \text{surface} \rightarrow r = 0.98R, \tag{38}$$

$$\mathrm{m} = \text{middle} \rightarrow r = 0.85R, \tag{39}$$

$$\mathrm{b} = \text{bottom} \rightarrow r = 0.72R, \tag{40}$$

and

$$\mathrm{np} = \text{northern hemisphere } 75^\circ < 90^\circ - \theta < 0^\circ, \tag{41}$$

$$\mathrm{eq} = \text{equator } 20^\circ < 90^\circ - \theta < -20^\circ, \tag{42}$$

$$\mathrm{sp} = \text{southern hemisphere } 0^\circ < 90^\circ - \theta < -75^\circ, \tag{43}$$

where θ is colatitude. So for example, $\langle \overline{B}_r \rangle_\mathrm{s}^\mathrm{eq}$ indicates the average of the azimuthally averaged B_r over $20^\circ < \theta < -20^\circ$, i.e. the equatorial, near the surface of the computational domain.

Typical density and temperature profiles are shown in Fig. 1, corresponding to the final state of *run20x*. The density at the bottom is 181.8 and 13.6 kg m^{-3} at the surface, where bottom and surface are evaluated following the definition in (38) and (40). This corresponds to a density

$$\frac{\rho_\mathrm{bottom}}{\rho_\mathrm{surface}} = 13.4. \tag{44}$$

The temperature profile is shown in the lower panel of Fig. 1. The temperature at the bottom is set to be the same as the temperature at the bottom of the CZ in the Sun, namely $T = 2 \times 10^6$ K, and decreases towards a value of 1.9×10^5 K at the surface.

The time-averaged angular velocity $\overline{\Omega} = \overline{u}_\phi / r \sin\theta + \Omega_0$ is shown from six latitudes from *run3x* in the top panel of Fig. 2. Overall the rotation is faster at the equator than at high latitudes, but we often observe an increase in the angular velocity at the latitude boundaries (see the cyan dotted lines in Fig. 2). This is likely an artefact due to the impenetrable latitude boundary. In the lower panel of Fig. 2, we show the time-averaged rotation profile for *run20x*. The difference in the rotation rates between high latitudes and the equator is significantly smaller than in the slower rotator. The decrease of differential rotation as the overall rotation rate is increased is consistent with earlier studies (e.g. Viviani et al. 2018).

At the beginning, the simulations first have to go through a relaxation phase during which thermal and magnetic saturation is established. The description that follows corresponds to *run20x*, but is qualitatively the same for *run3x*. There are two conditions that need to be fulfilled before analysing the results and deriving astrophysical implications for PCEB systems.

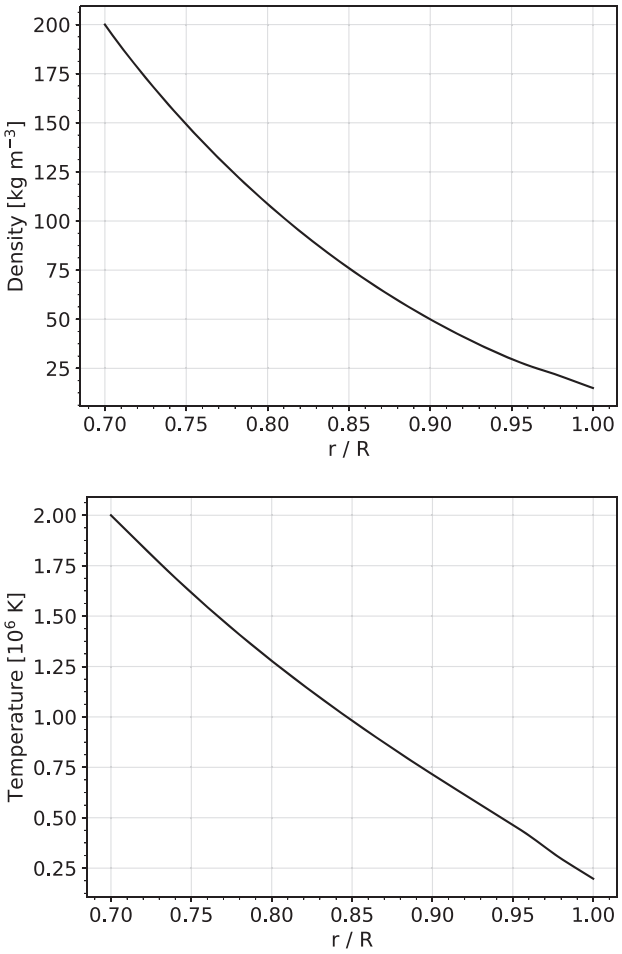

Figure 1. Density (top) and temperature profile (bottom) for *run20x*.

On the one hand, the system has to reach dynamo saturation, which is shown in Fig. 3, where we plot the root-mean-squared magnetic field for *run20x*. The seed magnetic field first decays because most of the initial magnetic energy is contained on the small scales which is quickly dissipated (Dobler, Stix & Brandenburg 2006). Furthermore, it takes susbtantial time for convection and large-scale flows to develop that lead to dynamo action. Subsequently, the magnetic field grows exponentially during the next three years during the kinematic stage. This growth starts to slow down in the non-linear regime until it reaches the saturation stage after about 22 yr.

The system has to also reach thermal equilibrium, which is shown in Fig. 4, where we plot the fraction of thermal to total energy. The only energy source in the simulations is the energy injected from the bottom of the CZ. While most of this energy is transported to the surface by convection, a fraction is deposited in the thermal reservoir of the CZ until equilibrium between energy input and output is achieved. This is manifested by an increase of the thermal energy in the present case. Thermal evolution after roughly eight years is slow and the system is sufficiently close to thermal saturation to be used for statistical analysis of the data.

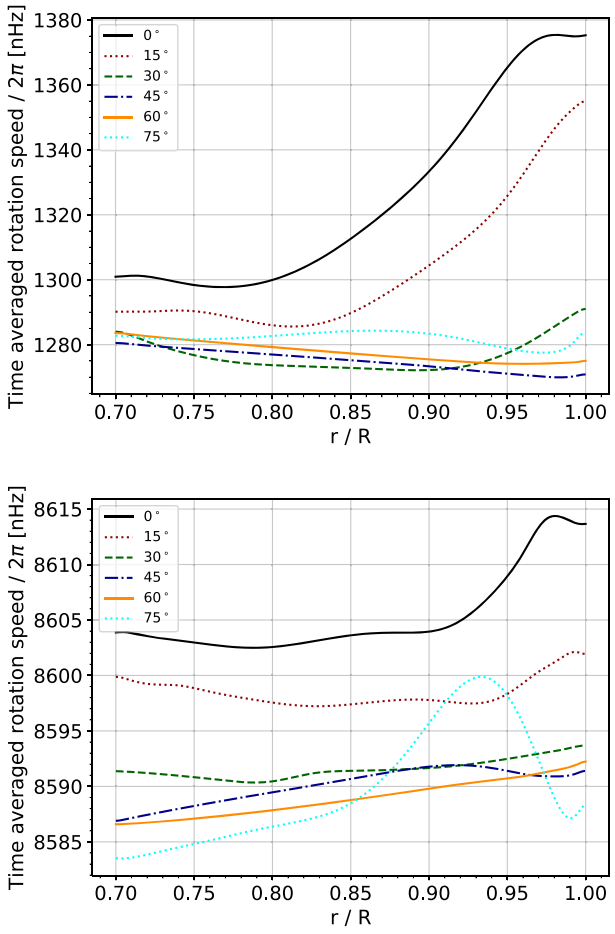

Figure 2. Angular velocity as a function of radius from six latitudes indicated by the legend from runs *run3x* (top) and *run20x* (bottom).

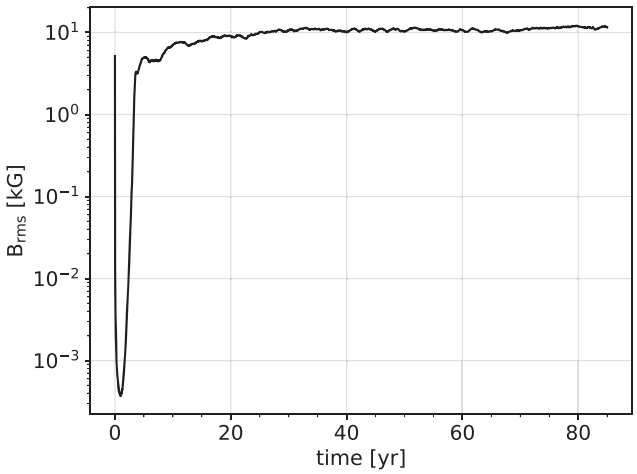

Figure 3. Saturation of the dynamo in *run20x*. The rms value of the magnetic field, $B_{\rm rms}$, grows exponentially up to the saturation regime where the analysis is performed.

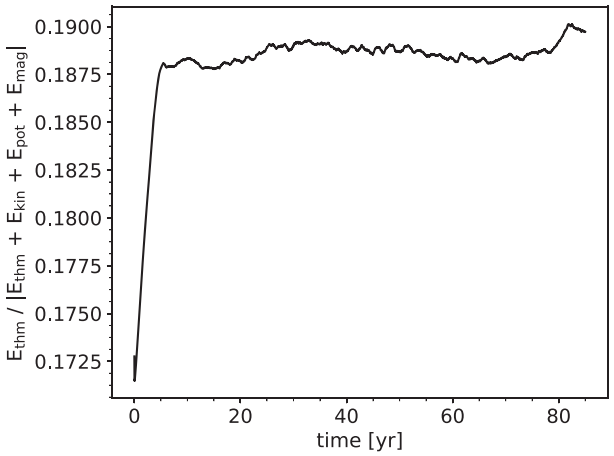

Figure 4. Evolution of the thermal energy as a fraction of the total energy of the system in *run20x*. $E_{\rm thm}$ is the thermal energy, $E_{\rm kin}$ is the kinetic energy, $E_{\rm pot}$ is the potential energy, and $E_{\rm mag}$ is the magnetic energy. The initial transient is due to the onset and maturing of convection and the corresponding development of turbulent heat transport.

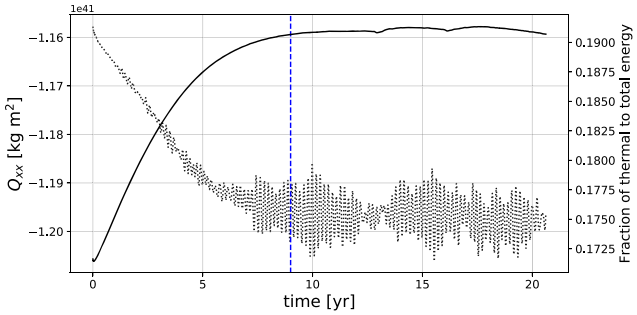

Figure 5. Gravitational quadrupole moment (Q_{xx}; dotted line) variations together with the thermal energy of the system (solid line). High-frequency oscillations are obtained. The thermal relaxation phase coincides with the phase of gravitational quadrupole moment relaxation, marked with the dashed blue line.

3.2 Purely hydrodynamical simulation

Here we present a pure hydrodynamical reference run with 20 times solar rotation. This serves essentially for comparison with the MHD simulations, to demonstrate that long-term variations only occur in simulations that include magnetic fields.

Fig. 5 shows the change of the gravitational quadrupole moment Q_{xx} in the dotted line, together with the thermal energy as a fraction of the total energy of the system as solid line. Here we can see very-high-frequency oscillations with a period of 0.18 yr. This is very close to an average sound-crossing time $\tau_{\rm sc}$, which we calculate as

$$\tau_{\rm sc} = \frac{2\,r_{\rm conv}}{\langle c_{\rm s}\rangle_{\rm vol}} \approx 0.18\,{\rm yr}, \tag{45}$$

where $r_{\rm conv}$ is the radial extent of the simulations, and $\langle c_{\rm s}\rangle_{\rm vol}$ corresponds to the sound speed, $c_{\rm s}$, averaged over the radial direction. The sound speed is calculated as

$$c_{\rm s} = \sqrt{\left(\frac{\partial p}{\partial \rho}\right)_s} \tag{46}$$

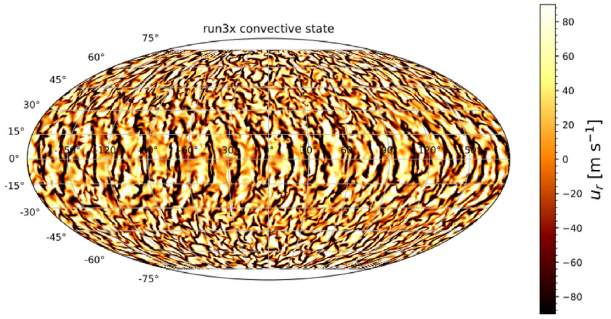

Figure 6. Radial velocity near the surface for *run3x*. The colour bar is cut at ± 90 m s^{-1} to improve visualization.

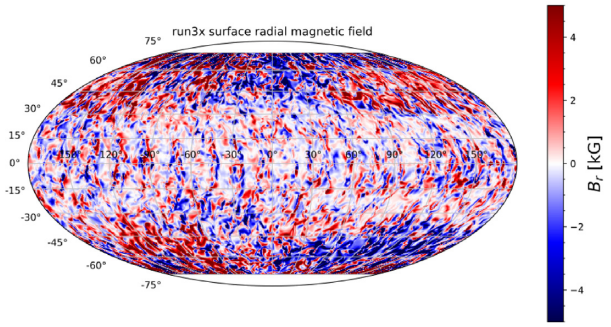

Figure 7. Radial magnetic field near the surface for *run3x*. The colour bar is cut at ± 5 kG to improve visualization.

where the subscript '*s*' indicates the derivative is taken at constant entropy. Thus, the high-frequency oscillations have a purely hydrodynamical origin.

3.3 The case of the slow rotator (*run3x*)

We first investigate the evolution of a simulation with three times solar rotation. This case is characterized by $\mathrm{Ta} = 5.68 \times 10^7$, $\mathrm{Co} = 2.68$, $\mathrm{Re} = \mathrm{Re}_M = 71$, $\mathrm{Pr}_M = 1$, and $\mathrm{Pr}_{\mathrm{SGS}} = 2.5$. Simulations with similar parameters were also explored by Viviani et al. (2018) for the stellar dynamo but they have not explored the implications on the stellar structure.

3.3.1 *Overview of convective and magnetic states*

To illustrate the general structure, we first examine a snapshot at the end of the simulation. Fig. 6 shows a Mollweide projection (an equal-area map projection also known as *homolographic projection*) of the near surface radial velocity. The colour bar is cut at ± 90 m s^{-1} to improve visualization. The velocity field does not show clear signs of large-scale structures. At the equator we see elongated cells (sometimes called 'banana cells'). Their existence is due to the influence that rotation has on the flow (see Busse 1970). At higher latitudes the banana cells disappear, and the effect of rotation is to give rise to more symmetric and smaller cells (see e.g. Chandrasekhar 1961). It should be noted that these cells are much larger than those observed in the Sun which is due to the much lower density stratification in the simulations. The mean radial velocity is ± 60 m s^{-1}, while the extrema can reach ± 1000 m s^{-1}.

In Fig. 7, we plot the near surface radial magnetic field at the end of the simulation. The colour bar is cut at ± 5 kG to improve visualization. The magnetic field strength at the equator is weaker than at high latitudes, and a clear $m = 1$ non-axisymmetric component is observed. The mean magnetic field strength is 2.5 kG and the extrema are ± 90 kG. The sizes of the magnetic structures is much larger than, e.g. sunspots. This is due to the fact that the current simulations lack the resolution to capture the small-scale granulation near the surface and the physics leading to spot formation.

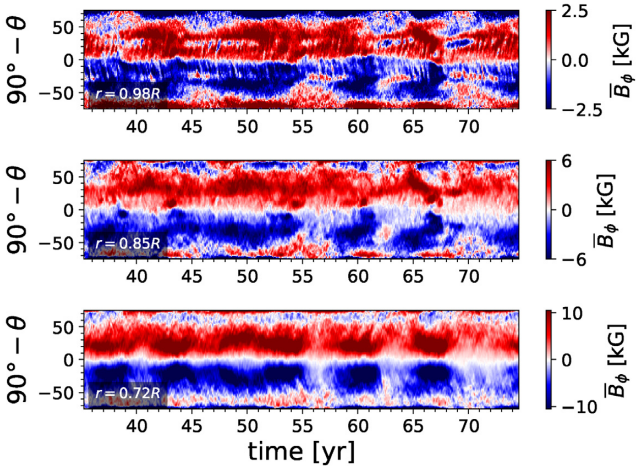

Figure 8. Time evolution of the mean toroidal magnetic field $\overline{B}_\phi$ for *run3x* at three different depths, labelled at the lower left corner of each panel. The magnetic field is changing its intensity and there are short periods where the activity is much weaker. The colour bars are cut to improve visualization.

3.3.2 *Overview of the magnetic field evolution*

We start the analysis by examining the dynamo solution of the slow rotator. Fig. 8 shows the evolution of the mean toroidal magnetic field (butterfly diagram) of *run3x* at three depths. At the Northern hemisphere there is an overall positive polarity whereas in the Southern hemisphere the dominant polarity is negative. In each panel, the polarity near the latitude boundaries is opposite to the dominant polarity. Polarity reversals can be seen at high latitudes at the bottom of the convective region (third panel). In the middle (second panel), these reversals at the poles are more pronounced and thus easier to see whereas at the surface the reversals are not as clearly observed in the azimuthal field. Thus, it appears that the axisymmetric part of the magnetic field consists of a dominant quasi-stationary component and a weaker quasi-periodic one, as also recently reported by Viviani et al. (2019). Meanwhile, the strength of the azimuthal magnetic field is varying quasi-periodically without polarity reversals near the equator. At the three reference depths there are episodes of decreased activity, for example at the equator during the time frames of 55 to 59 yr and 62 to 66 yr. The extrema at the bottom, middle, and surface are ± 20, ± 7, and ± 3 kG, respectively.

The evolution of the radial field is shown in Fig. 9. At the bottom of the convective zone (bottom panel) the behaviour of $\overline{B}_r$ is similar to the one described for the toroidal field at the surface. At low latitudes and towards the equator the magnetic field is positive (negative) at the Northern (Southern) hemisphere, and there are no clear signs of polarity reversals. In the middle of the convective region we start seeing hints of a poleward migrating dynamo wave (see second panel in Fig. 9) at latitudes greater than 50° in both hemispheres. Meanwhile, at mid-latitudes ($\pm 30°$) a persistently negative (positive) magnetic field in the Northern

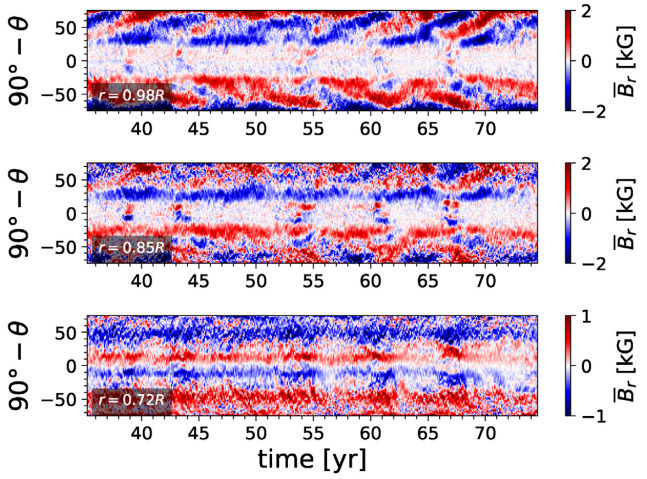

Figure 9. Time evolution of the mean radial magnetic field $\overline{B}_r$ for *run3x* at three different depths, labelled at the lower left corner of each panel. A poleward migration of the magnetic field is clearly seen at the surface of the domain. Sporadic activity is seen at the equator.

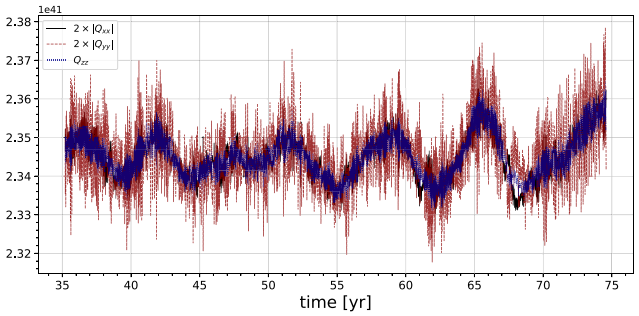

Figure 10. Time evolution of the gravitational quadrupole moment components $2|Q_{xx}|$, $2|Q_{yy}|$, and Q_{zz} in *run3x*. Apart from differences of a factor of approximately two, the components follow the same overall trend, in the form of short-term differences in the high-frequency oscillations.

(Southern) hemisphere is obtained with no migration. Near the equator, the mean radial magnetic field is weaker but with periods of increased strength at $t = 39$, 43, 55, 51, and 67 yr. At the surface of the star (top panel) a dynamo wave is obtained with a poleward migration. At the equator the strength of $\overline{B}_r$ is weaker with periods of increased strength at the same times as in the middle of the computational domain.

3.3.3 *Origin of the quadrupole moment fluctuations*

The time evolution of the diagonal elements of the quadrupole moment Q_{xx}, Q_{yy}, and Q_{zz} is shown in Fig. 10. While Q_{zz} is positive, Q_{xx} and Q_{yy} are negative, and there is a difference of about a factor of two in the components. Apart from that, their overall behaviour is very similar, showing a quasi-periodic evolution with a period of around eight years, and an amplitude of the order of $\sim 1 \times 10^{39}$ kg m^2 in the case of Q_{xx}. For comparison, we also applied the semi-analytic model by Völschow et al. (2018), obtaining the same order of magnitude for the fluctuations. The system further shows the presence of short-term oscillations, which are also present in hydrodynamical runs (see Section 3.2). We will in the following text take the Q_{xx} component as a reference that we compare to other

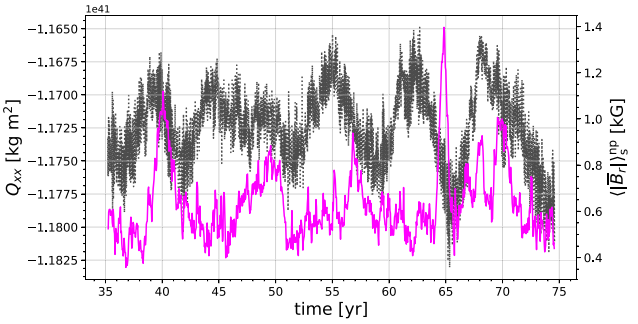

Figure 11. Time evolution of the gravitational quadrupole moment component Q_{xx} (black dotted line) in *run3x* together with the absolute value of the azimuthal average of the radial magnetic field near the surface averaged over the Northern hemisphere (magenta solid line). The variations of Q_{xx} can be interpreted as a reaction to the changes of the magnetic field intensity (see the text).

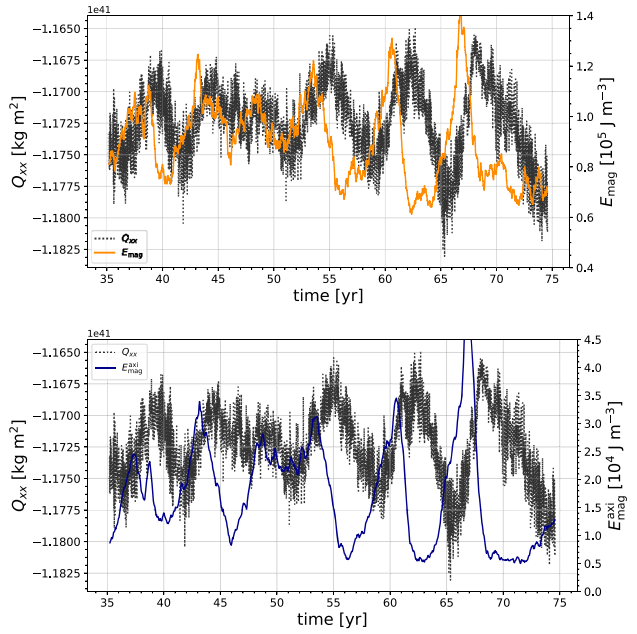

Figure 12. Time evolution of the total magnetic energy (top panel) and the axisymmetric magnetic energy (lower panel), compared to the evolution of the gravitational quadrupole moment Q_{xx} (black line) in run3x.

quantities, keeping in mind that the result would be similar for the other components as well.

We compare the evolution with the average radial magnetic field near the surface averaged over the Northern hemisphere in Fig. 11. We can see peaks of the magnetic field and how they relate to the quadrupole moment. The first peak of the magnetic field at $t =$ 40 yr can be related to the minimum of Q_{xx} at $t = 41.7$ yr. Then, the continuous increase in the magnetic field intensity from $t =$ 45 yr to $t = 50$ yr is reflected in a decrease of Q_{xx} starting at the 45 yr mark to $t = 51$ yr. This shows the direct impact of magnetic field to the overall density distribution of the star. We also compare the evolution of Q_{xx} directly with the evolution of the total and axisymmetric magnetic energies in the top and bottom panels of Fig. 12. Here we see a close anticorrelation between the magnetic energy and Q_{xx} in both panels, and a time lag might also be present.

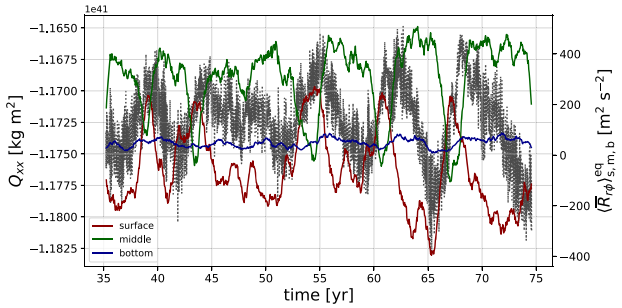

Figure 13. Time evolution of the gravitational quadrupole moment component Q_{xx} (black line) in *run3x* together with the mean averaged of the Reynolds stress component $\overline{R}_{r\phi}$ at the equator in the surface (red), middle (green), and bottom (blue).

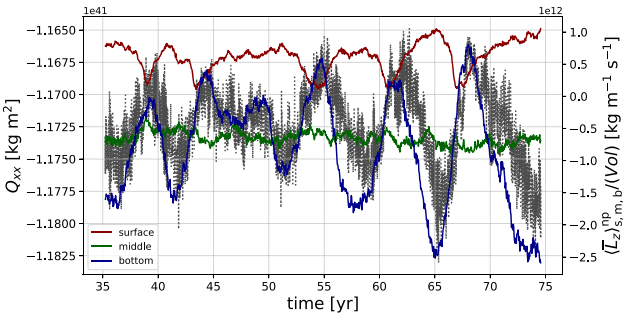

Figure 14. Time evolution of the gravitational quadrupole moment component Q_{xx} (black dotted line) together with the angular momentum per unit volume averaged over the Northern hemisphere at the surface (red), middle (green), and bottom (blue) for *run3x*.

Now, we explore the correlation between the Reynolds stress tensor component $\overline{R}_{r\phi} = \overline{u'_r u'_\phi}$, where primes denote fluctuations from azimuthal averages which are denoted by overbars, which is known to drive differential rotation (Rüdiger 1989; Käpylä et al. 2016). This is shown in Fig. 13. The stress at the surface (middle) of the computational domain is correlated (anticorrelated) with the quadrupole moment. The stress at the bottom is weak and with a small contribution and weak correlation to Q_{xx}.

Finally, we study how the angular momentum $L_z = \overline{\rho}\varpi^2\overline{\Omega}$, where $\varpi = r\sin\theta$ is related to Q_{xx}. In Fig. 14, we plot the angular momentum per unit volume averaged over the Northern hemisphere at the surface (red), middle (green), and bottom (blue). While the angular momentum itself will not directly affect the stellar structure through the centrifugal force, it changes due to the Reynolds stress and shows a strong correlation here with the change of the quadrupole moment.

From this figure, we see that the outer layers carry less angular momentum than the inner ones, and at the surface there is an anticorrelation between the absolute value of Q_{xx} and the absolute value of L_z. The angular momentum at the surface further appears to be anticorrelated with the angular momentum in the middle and at the bottom, thus indicating an internal redistribution.

3.3.4 Gravitational quadrupole moment evolution

We return to Fig. 10 to analyse the time evolution of quadrupole moment. We are interested in variations on time-scales longer than the hydrodynamic oscillations with a period of ∼0.18 yr, see Section 3.2. The variations in Q_{xx} are not strictly periodic. For example, there is an episode between $t \sim 44$ and $t \sim 52$ yr where it takes clearly more time to reach a local maximum. Furthermore, Q_{xx} reaches a global minimum at $t = 65$ yr which is clearly lower than those that precede it. This behaviour is to be expected to a certain degree as the full set of MHD equations is highly non-linear. Overall, these fluctuations have a period of approximately five to six years and semi-amplitudes of $\sim 1 \times 10^{39}$ kg m^2.

Bearing in mind the necessary rescaling to obtain astrophysical values (see Section 2.4) and that we are modelling a solar mass star, we can use the results from our simulations to estimate the impact in V471 Tau. Following Applegate (1992), the variations in the binary period are related to variations in the quadrupole moment via

$$\frac{\Delta P}{P} = -9\left(\frac{R}{a_{\rm bin}}\right)^2 \frac{\Delta Q_{xx}}{MR^2}, \tag{47}$$

or

$$\frac{\Delta P}{P} = -9\frac{\Delta Q_{xx}}{M a_{\rm bin}^2}, \tag{48}$$

where M and R are the mass and radius of the magnetically active star, and $a_{\rm bin}$ is the binary separation. We take the Q_{xx} semi-amplitude as

$$\Delta Q_{xx} = 1 \times 10^{39}\ {\rm kg\ m^2} \tag{49}$$

and adopt a binary separation of 3.3 $R_\odot$. This result is consistent with the semi-analytic model by Völschow et al. (2018), adopting fluctuations of about 10 per cent in the turbulence and magnetic field. We therefore obtain

$$\frac{\Delta P}{P} = 8.4 \times 10^{-10}. \tag{50}$$

Furthermore,

$$O - C = \frac{\Delta P}{P}\frac{P_{\rm mod}}{2\pi}, \tag{51}$$

where $P_{\rm mod}$ is the modulation period of the $O - C$ diagram (see Applegate 1992). Combining this equation with equation (48) yields

$$O - C = 0.025\ {\rm s}. \tag{52}$$

Marchioni et al. (2018) presented the most updated analysis of the eclipsing times of V471 Tau. The authors reported two period variations, one with $O - C = 151$ s and $P_{\rm mod} = 35$ yr. The other contribution has a semi-amplitude of $O - C = 20$ s and a modulation period of $P_{\rm mod} = 9.7$ yr. The semi-amplitude obtained from the simulations in this case is thus much lower than observed. However, we note that the rotation rate is different than in V471 Tau, and also the stellar mass may not be exactly the same. Indeed, more promising results will be obtained with the fast rotator in the next section.

3.4 The case of the fast rotator (*run20x*)

We now investigate the evolution of a simulation with 20 times solar rotation. This case is characterized by Ta $= 2.55 \times 10^9$, Co $= 59.7$, Re $=$ Re$_M = 21$, Pr$_M = 1$, and Pr$_{\rm SGS} = 2.5$. Also this simulation lies within the parameter regime explored by Viviani et al. (2018).

3.4.1 Overview of convective and magnetic states

Fig. 15 shows the near-surface radial velocity from *run20x*. Also here, banana cells are present at the equator, but with a decreased

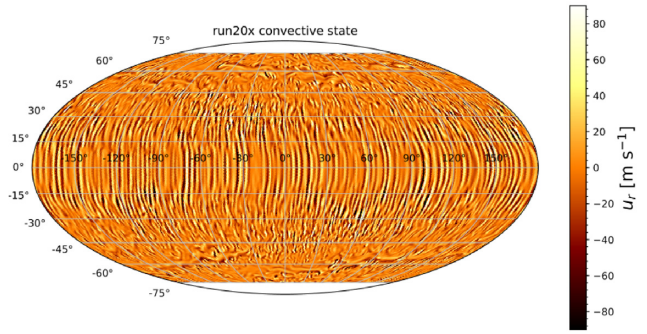

Figure 15. Mollweide projection of the radial velocity near the surface for *run20x*. The colour bars are cut to improve visualization.

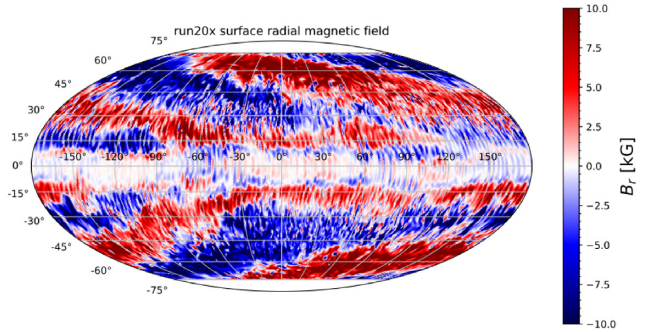

Figure 16. Mollweide projection of the radial magnetic field near the surface for *run20x*. The colour bars are cut to improve visualization.

azimuthal extent in comparison to *run3x*. At higher latitudes the size of the convection cells is also reduced. This decreasing size of convection cells as the rotation increases is in accordance with linear stability analysis (e.g. Chandrasekhar 1961) and earlier numerical simulations (e.g. Viviani et al. 2018). The average convective velocity is 19.4 m s^{-1}, with extrema of 700 and −561 m s^{-1}.

Fig. 16 shows the near-surface radial magnetic field at the end of *run20x*. The radial magnetic field differs from that of *run3x* in that it is stronger and more organized. The rms radial magnetic field is 4.5 kG, i.e. 1.8 times stronger than in *run3x*. The extrema are about ±90 kG, as in *run3x*. These large-scale magnetic structures can cover the whole surface of the star. A possible explanation is that convection in the rapidly rotating run is less supercritical in terms of its Rayleigh number because the values of ν and $\chi_{\rm SGS}$ remain the same as in *run3x*. Thus the flows and magnetic fields in *run20x* are more laminar than in *run3x*.

3.4.2 *Overview of the magnetic field evolution*

We follow here the same approach as in the case of the slow rotator. Fig. 17 shows the time evolution of the mean toroidal magnetic field, i.e. butterfly diagram, at three depths labelled at the lower left corner of each panel. The mean magnetic field shows a more complex behaviour than in *run3x*. At the bottom of the domain the dynamo solution is cyclic everywhere in the beginning. The maximum amplitudes are ±12 kG. At later times there is a quasi-stationary axisymmetric magnetic field from 57 to 76 yr, covering most of the Southern hemisphere. The dynamo solution at the middle of the domain is persistently cyclic with a poleward migration. Here the extrema of the magnetic field are ±8 kG. At the surface there is a poleward dynamo wave near the equator with

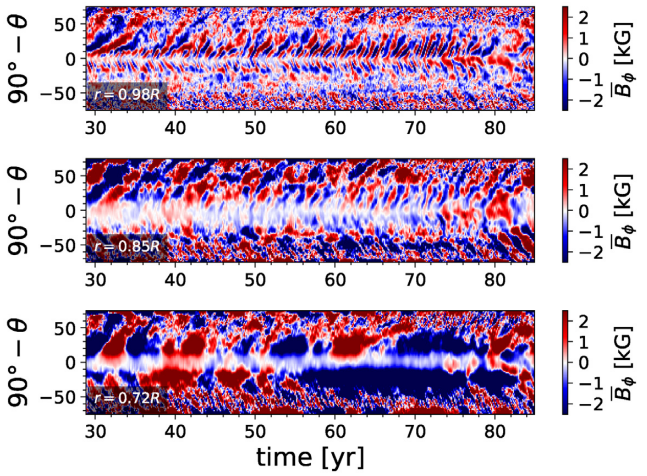

Figure 17. Time evolution of the mean azimuthal toroidal magnetic field $\overline{B}_\phi$ for *run20x*. A poleward migration of the magnetic field is clearly seen at the surface and middle of the domain. Near the equator there is a hemispheric wave operating on the Northern hemisphere at latitudes between ∼5° to ∼50°. This hemispheric asymmetry is decreasing towards the end of the simulation. The colour bars are cut at ±2.5 kG for better visualization.

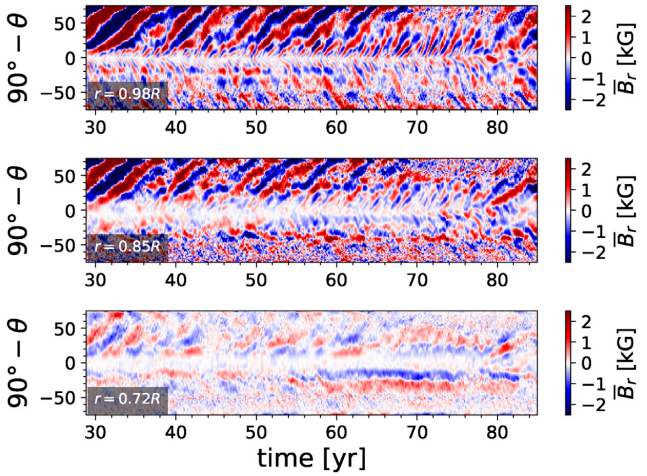

Figure 18. Time evolution of the mean radial magnetic field $\overline{B}_r$ for *run20x*. The hemispheric dynamo wave is clearly seen at the surface and middle of the domain. It is also seen that the magnitude of the axisymmetric field decreases until around 70 yr.

extrema of ±5 kG. This poleward mode is clearly more coherent on the Northern hemisphere and can be seen at latitudes between ∼5° to ∼50°, whereas a higher frequency wave on the Southern hemisphere can be seen only very near the equator. The amplitude of the axisymmetric magnetic field is also slowly decreasing during the simulation. The absence of a strong toroidal magnetic field near the surface is due to the radial field boundary condition (see Käpylä et al. 2016; Warnecke et al. 2016).

A time-latitude diagram for $\overline{B}_r$ is shown in Fig. 18. Here, the presence of a hemispheric dynamo wave with decreasing amplitude in time is clearly visible and the magnetic fields have a poleward migration. At early times, the extrema at the surface (bottom) is ±20 kG (±8 kG). The hemispheric asymmetry disappears in the period between 68 to 80 yr and the extrema near the top (bottom) is ±4 kG (±3 kG), respectively. The behaviour is quite different from the case of *run3x*. This is because the excited dynamo mode

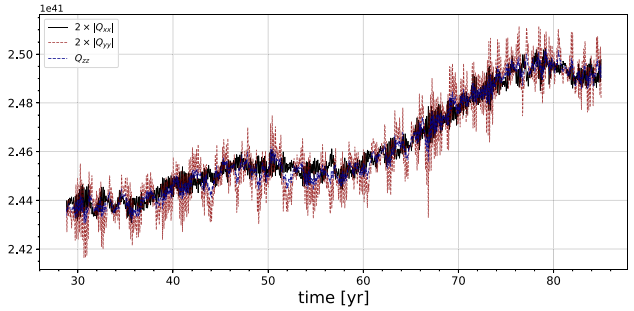

Figure 19. Time evolution of the gravitational quadrupole moment components $2|Q_{xx}|$, $2|Q_{yy}|$, and Q_{zz} in *run20x*. Apart from differences of a factor of approximately two, the components follow the same overall trend, with short-term differences in the high-frequency oscillations.

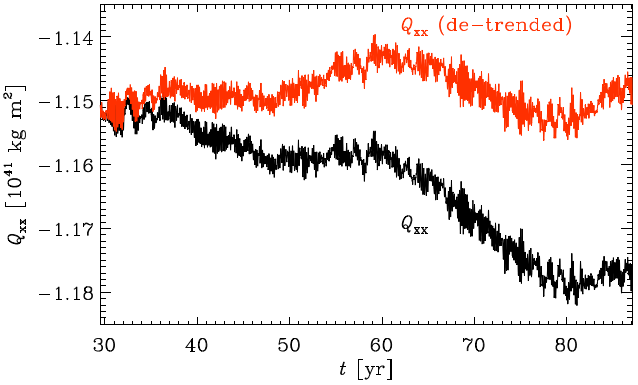

Figure 20. Total and detrended Q_{xx} in black and orange, respectively, for *run20x*.

depends on the rotation rate of the simulation (see e.g. Viviani et al. 2018). The major differences in the magnetic field evolution between *run3x* and *run20x* is that first, the intensity of $\overline{B}_r$ in the latter is larger by a factor of two at the surface. Secondly, the overall intensity of the azimuthally averaged magnetic field in the latter is decaying, whereas in *run3x* it remains roughly constant. And thirdly, the magnetic field is migrating virtually everywhere in *run20x*, whereas the migrating component was found to be subdominant in *run3x* where a strong quasi-steady field is present at all times (see Fig. 9). We note in summary that the behaviour of the magnetic field is considerably more complex in the rapidly rotating case.

3.4.3 *Origin of the* Q_{xx} *fluctuations*

Analogous to the slowly rotating case, we explore the origin of the quadrupole moment variations. The time evolution of the diagonal elements Q_{xx}, Q_{yy}, and Q_{zz} are shown in Fig. 19 but we again study Q_{xx} bearing in mind that the result would be similar for the other components. In $|Q_{xx}|$, we see a quasi-periodic variation on a timescale of about 30 yr superimposed with a longer term trend. The latter, which decreases continuously the quadrupole moment, might be related to an incomplete thermal saturation of the stellar interior. For this reason, we have detrended Q_{xx} by taking the difference between the endpoints of its time series and subtracting this linear trend from the data. The resulting time series is shown in Fig. 20. We first compare the total, non-detrended Q_{xx} to the evolution of the mean radial magnetic field averaged at the Northern hemisphere at the surface of the domain, depicted in Fig. 21. The sharp decrease

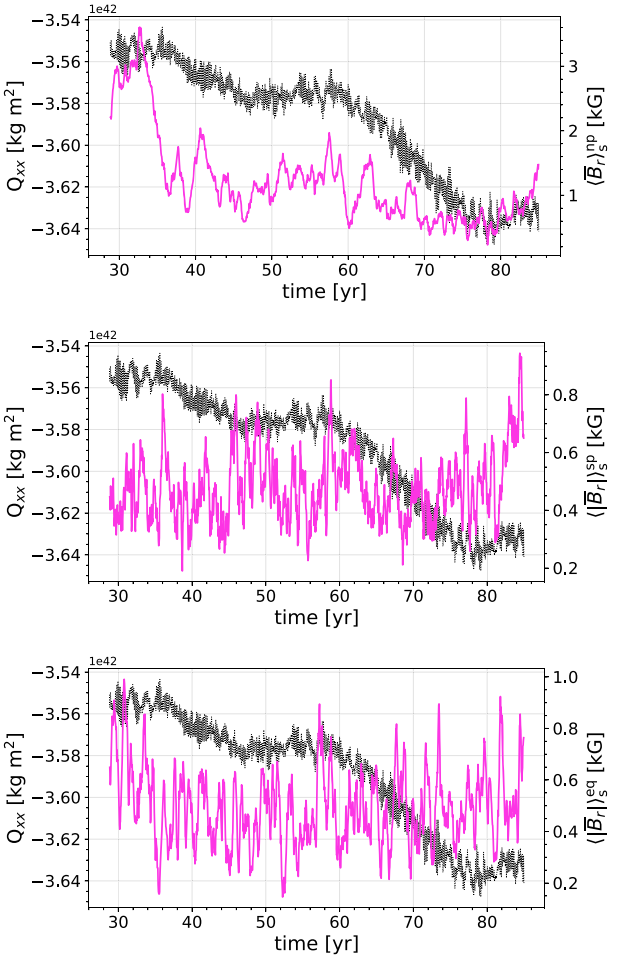

Figure 21. Time evolution of the gravitational quadrupole moment component Q_{xx} (black dotted line) for *run20x* together with the absolute value of the mean radial magnetic field averaged at the North pole (top panel) in the surface of the domain (magenta solid line). The middle panel shows the comparison with the mean radial magnetic field averaged at the South pole in the surface of the domain, in the bottom panel the average was taken at the equator in the surface of the domain.

of $\langle \overline{B}_r \rangle_s^{np}$ reflects the change in the dominant dynamo mode (same as in Fig. 18). The effect of this decrease on Q_{xx} can also be clearly seen.

This correlation is not seen when the same quantities are compared on the Southern hemisphere (see middle panel of Fig. 21). It can also be seen that the mean magnetic field is weaker by almost an order of magnitude in the Southern hemisphere around $t = 32$ yr. The mean field strengths evolve gradually such that they are equal around $t = 70$ yr. The mean fields at both hemispheres start to grow around the 80 yr mark; see top panel of Fig. 21) which coincides with the weak increase in Q_{xx}. Finally, it can be seen from the bottom panel of Fig. 21 that the average magnetic field at the equatorial portion of the surface of the star does not have significant variations nor correlation with Q_{xx}. We further compare the evolution of the *detrended* Q_{xx} with the total magnetic and the azimuthal magnetic energy in Fig. 22. Here, especially for the azimuthal magnetic energy, the anticorrelation is less pronounced than we previously found in run *run3x*. In the total magnetic energy, several maxima or minima show counterparts in the evolution of Q_{xx}

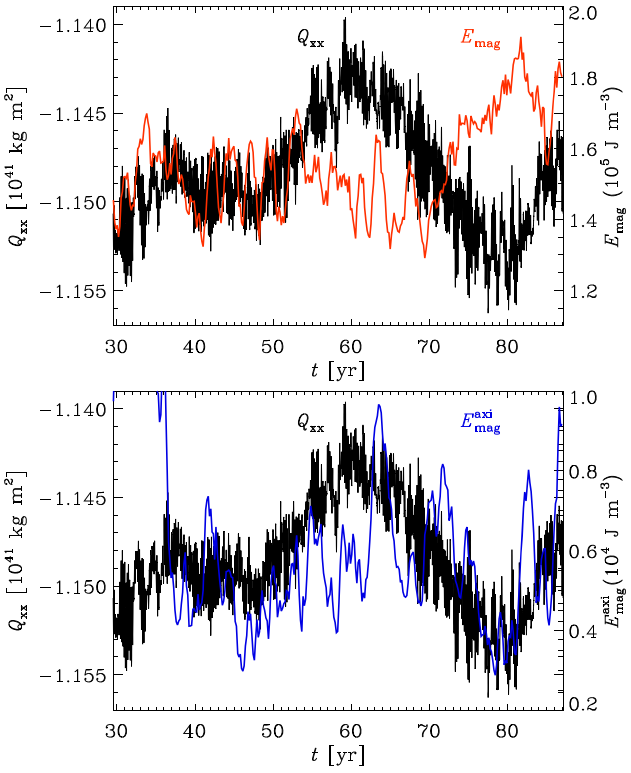

Figure 22. Time evolution of the total magnetic energy (top panel) and the axisymmetric magnetic energy (lower panel), compared to the evolution of the detrended gravitational quadrupole moment Q_{xx} (black line) in *run20x*.

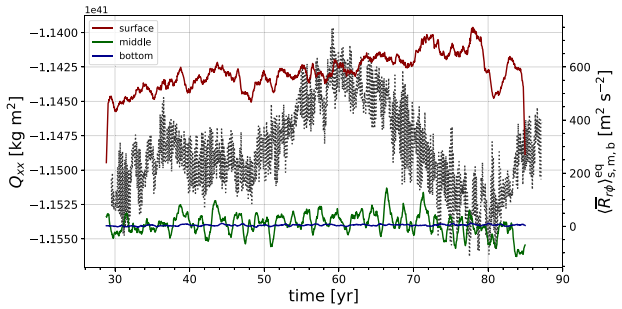

Figure 23. Time evolution of the gravitational quadrupole moment component Q_{xx} (black dotted line) for *run20x* together with the mean averaged Reynolds stress component $R_{r\phi}$ at the equator in the surface (red line), middle (green), and bottom (blue) of the domain.

but only towards the end of the simulation, i.e. $t \gtrsim 65$ yr. Further, while Q_{xx} on average is decreasing during the period investigated here, the total magnetic energy shows an average increase. The azimuthal magnetic energy, on the other hand, shows a strong peak towards the beginning of the simulated period, and subsequently remains at a lower level with quasi-periodic fluctuations on a timescale of roughly five years in superposition with a possible longer term modulation.

As for *run3x*, we plot the $r\phi$ component of the Reynolds stress at the equator and at the three depths in Fig. 23. The average of $\overline{R}_{r\phi}$ at the surface is steadily increasing while Q_{xx} decreases. Meanwhile, the stress at the deeper layers is approximately constant. There is anticorrelation between Q_{xx} and the stress at the equator

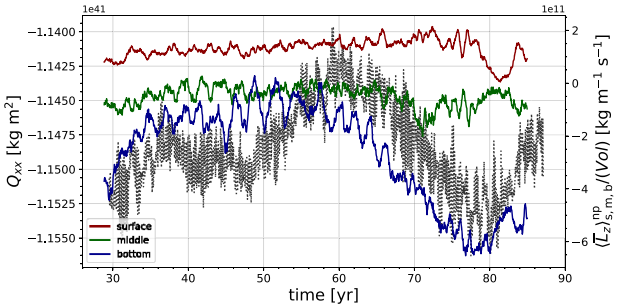

Figure 24. Time evolution of the gravitational quadrupole moment component Q_{xx} (black dotted line) for *run20x* together with the angular momentum per unit volume averaged over the Northern hemisphere at the surface (red), middle (green), and bottom (blue) for the fast rotator.

near the surface in the latter part ($t \gtrsim 60$ yr) of the simulation. We also show the correlation between the quadrupole moment and the angular momentum at three depths in Fig. 24, though we note as before that this correlation is due to the effect of angular momentum redistribution by the Reynolds tensor, and unrelated to the centrifugal acceleration. While at early times L_z at the bottom increases and Q_{xx} remains constant, the correlation in both quantities after the 40 yr mark is high. To recapitulate, we find that the evolution of the fast rotator is much more complex in comparison to the more slowly rotating counterpart and clear correlations between magnetic activity and quadrupole moment variations are visible only towards the end of the simulation. A significantly longer time series would be needed to quantify this effect more precisely. This is out of the scope of this study and will be pursued elsewhere.

3.4.4 *Gravitational quadrupole moment evolution*

The purely hydrodynamic oscillations in the quadrupole moments particularly Q_{xx} (see also Section 3.2) are present, similarly as in *run3x*. The overall behaviour of the quadrupole moment in this run is remarkably different from the case of *run3x*, showing a more complex behaviour. At the beginning from the 29 to 37 yr marks Q_{xx} remains constant on average, apart from the presence of hydrodynamic oscillations with a period of ∼0.18 yr. After the 37 yr mark, Q_{xx} decreases gradually from -1.15×10^{41} to -1.16×10^{41} kg m^2. After this, the behaviour described above starts again but now the decrease is stronger and starts at 60 yr. Q_{xx} changes from -1.17×10^{41} to -1.18×10^{41} kg m^2. It is thus possible that we see here a quasi-periodic oscillation superimposed with a longer term trend. Analogous to the case of *run3x* where we rescaled the gravitational quadrupole moment (see Section 2.4), we take the system parameters of the magnetically active component in the PCEB V471 Tau and bear in mind that this run has a rotation rate and stellar parameters similar to the magnetically active star in this system, but now we take the maximum and minimum of Q_{xx} to obtain

$$\Delta Q_{xx} = 1.7 \times 10^{39}\,\mathrm{kg\,m^2} \tag{53}$$

and adopt a binary separation of 3.3 $R_\odot$. Inserting this into equation (48) yields

$$\frac{\Delta P}{P} = 1.40 \times 10^{-9}. \tag{54}$$

Furthermore,

$$O - C = \frac{\Delta P}{P} \frac{P_{\rm mod}}{2\pi} \tag{55}$$

where $P_{\rm mod}$ is the modulation period of the $O - C$ diagram semi-amplitude (see Applegate 1992) with equation (48). In our case $P_{\rm mod} = 50$ yr. Thus

$$O - C = 0.13\,{\rm s}. \tag{56}$$

The semi-amplitude obtained from the simulations is still lower than the observed value found by Marchioni et al. (2018). Nevertheless, we also found that it has increased considerably compared to the slow rotator, by a factor of 5.2, while the rotation velocity has changed by roughly a factor of 6.7. As we are still a factor of 2.5 below the rotation velocity of V471 Tau, it is conceivable that another significant increase could be expected for the parameters of that system. In addition, we note that the centrifugal force is neglected in our simulations, which can be another relevant contribution.

4 DISCUSSION AND CONCLUSIONS

In this paper, we have studied the stellar quadrupole moment variations arising from magnetic activity through directly solving the 3D compressible non-ideal MHD equations with the PENCIL CODE. We have run two simulations of solar mass stars, one with three times the solar rotation rate, and the other with 20 times solar rotation. This is motivated by the fact that typical rotation rates in PCEBs are considerably higher than for isolated stars. As a reference system, we here consider V471 Tau, which has a roughly solar mass secondary.

In the two simulations we have run, we see two very different behaviours in the evolution of the magnetic fields and the quadrupole moment. For the slow rotator, quasi-periodic oscillations in the quadrupole moment, the magnetic field, the Reynolds stress, and other quantities can be distinguished easily. Meanwhile, for the fast rotator the evolution is much more complex, which can also be seen in the magnetic field evolution. The slow rotator has a relatively simple magnetic field behaviour, showing a superposition of a strong quasi-steady and a weaker migrating dynamo modes, whereas the fast rotator has a significantly more complex magnetic field evolution. It has a poleward migrating magnetic field near the equator and a superposed hemispheric dynamo wave operating only on the Northern hemisphere. The latter is also decreasing its amplitude. While the run has been evolved for a total of 90 yr, it may not yet be in complete thermal saturation, which can give rise to the long-term trends that we observed. We therefore have detrended the simulations to correct for such an influence, yielding then a clear anticorrelation with magnetic energy.

We have established a link between the magnetic activity and the gravitational quadrupole moment by means of the Reynolds stress tensor, which will be affected by the magnetic dynamo due to its local effect on the convective velocities. There is an anticorrelation between both the total and axisymmetric magnetic energies and Q_{xx}, but we do not discard a time lag of the anticorrelation. While in the case of the slow rotator it is relatively easy to observe, in the fast rotator case the behaviour is much more complex, as it shows signs of a quasi-periodic change, on which a global trend appears to be superimposed both for the magnetic field and the quadrupole moment. The timeline in our simulations (∼55 yr) is larger than the observed timeline in V471 Tau, while the observed timeline corresponds to about 35 yr. The expected $O - C$ variation has increased considerably going from the slow to the fast rotator, where a change by half an order of magnitude in the rotation velocity corresponds to a change by a factor of 5.2 in the expected value of $O - C$. As even the fast rotator is a factor of 2.5 below the rotation velocity of V471 Tau, another significant increase may be expected for the rotation velocity of that system. We also note that the effect of the centrifugal force has been neglected so far, but it may further enhance the $O - C$ variations. The current simulations also assume a fixed spherically symmetric gravitational potential. This modelling choice is possibly also limiting the quadrupole moment variations.

Overall, we arrive at the following preliminary conclusions:

(i) the complexity of the evolution of Q_{xx} is linked to the dynamo mode, angular momentum evolution, and Reynolds stress tensor,
(ii) Q_{xx} is anticorrelated to the total and axisymmetric magnetic energies,
(iii) the numbers of the $O - C$ amplitude and $\Delta P/P$ depend on the overall magnetic field evolution and complexity,
(iv) the angular momentum at the bottom of the CZ is more correlated to Q_{xx} than that near the surface,
(v) ΔQ_{xx} has a dependence on stellar rotation.

In spite of relevant uncertainties to be explored, we present here the first analysis showing how the stellar quadrupole moment changes as a function of time in compressible non-ideal MHD simulations. We find strong evidence that magnetic effects can indeed produce such variations, while pure hydrodynamical runs as presented in Section 3.2 produce only short-term variations on the sound-crossing time-scale. We believe that such simulations will be important in the future to more quantitatively explore the effects of magnetic activity in close binary systems, and to allow a better understanding of the observed phenomena.

The variations in Q_{xx} found here should be taken as indicative rather than precise, as with the current computational power it is impossible to approach the *real* dimensionless parameters that govern stellar plasmas. For example, the magnetic Prandtl number is 1 in the simulations whereas in the Sun it is $\sim 10^{-5}$. The normalized flux in the bottom of the Sun is $\sim 10^{-11}$ whereas in the simulation it is highly enhanced with a value of 3.2×10^{-5}. In the case of the Reynolds number this is more severe, as in the Sun it ranges from 10^{12} to 10^{13} and in the simulations we have Re $\sim$ 21–71. However, the simulations in previous studies have proven to be successful in reproducing some of the solar phenomena (see e.g. Käpylä, Mantere & Brandenburg 2012; Käpylä et al. 2013, 2016; Viviani et al. 2018). Further development of 3D MHD simulations of fully convective stars will prove to be of great importance as we expect the Applegate mechanism to be an important tool for studying dMs dynamos through eclipsing time variations.

To draw stronger conclusions, more simulations are required to explore the parameter space. In particular, exploring how Q_{xx} depends on stellar rotation and mass is important as the magnetically active companion in PCEBs is rotating at a high fraction of their critical stellar rotation, which scales with the energetical feasibility of the Applegate mechanism (Navarrete et al. 2018). Also, fully convective stars are expected to produce a higher amplitude of $\Delta P/P$ based on the models of Völschow et al. (2018). Based on such simulations, eclipsing time observations may become a promising tool to probe stellar dynamos in the future.

ACKNOWLEDGEMENTS

FHN acknowledges financial support from CONICYT (project code CONICYT-PFCHA/Magister Nacional/22181506). DRGS

and FHN thank for funding through FONDECYT regular (project code 1161247) and through the 'Concurso Proyectos Internacionales de Investigación, Convocatoria 2015" (project code PII20150171). REM and DRGS acknowledge FONDECYT regular 1190621 and the BASAL Centro de Astrofísica y Tecnologías Afines (CATA) PFB-06/2007. We acknowledge the Kultrun Astronomy Hybrid Cluster (projects Conicyt Programa de Astronomia Fondo Quimal QUIMAL170001, Conicyt PIA ACT172033, Fondecyt Iniciacion 11170268 and BASAL Centro de Astrofísica y Tecnologías Afines (CATA) PFB-06/2007) for providing HPC resources that have contributed to the research results reported in this paper. Powered@NLHPC: This research was partially supported by the supercomputing infrastructure of the NLHPC (ECM-02). PJK was supported by the Deutsche Forschungsgemeinschaft Heisenberg programme (grant no. KA 4825/1-1), and the Academy of Finland ReSoLVE Centre of Excellence (grant No. 307411). Part of the simulations were performed using the supercomputers hosted by CSC – IT Center for Science Ltd. in Espoo, Finland, who are administered by the Finnish Ministry of Education. JS acknowledges funding from the European Union's Horizon 2020 research and innovation program under the Marie Skłodowska-Curie grant No. 665667.

REFERENCES

Applegate J. H., 1992, ApJ, 385, 621
Bear E., Soker N., 2014, MNRAS, 444, 1698
Berdyugina S. V., Henry G. W., 2007, ApJ, 659, L157
Beuermann K. et al., 2010, A&A, 521, L60
Beuermann K. et al., 2012, A&A, 540, A8
Beuermann K., Dreizler S., Hessman F. V., 2013, A&A, 555, A133
Bours M. C. P. et al., 2014, MNRAS, 445, 1924
Bours M. C. P. et al., 2016, MNRAS, 460, 3873
Brandenburg A., 2003, Computational Aspects of Astrophysical MHD and Turbulence, Taylor and Francis, London, p. 269
Brandenburg A., Dobler W., 2002, Comput. Phys. Commun., 147, 471
Brandenburg A., Chan K. L., Nordlund Å., Stein R. F., 2005, Astron. Nachr., 326, 681
Brinkworth C. S., Marsh T. R., Dhillon V. S., Knigge C., 2006, MNRAS, 365, 287
Busse F. H., 1970, ApJ, 159, 629
Chandrasekhar S., 1961, Hydrodynamic and Hydromagnetic Stability, International Series of Monographs on Physics, Oxford University Press, Oxford
Cole E., Käpylä P. J., Mantere M. J., Brandenburg A., 2014, ApJ, 780, L22
Dobler W., Stix M., Brandenburg A., 2006, ApJ, 638, 336
Donati J.- F. et al., 2003, MNRAS, 345, 1145
Goździewski K. et al., 2012, MNRAS, 425, 930
Goździewski K. et al., 2015, MNRAS, 448, 1118
Hardy A. et al., 2015, ApJ, 800, L24
Hinse T. C., Lee J. W., Goździewski K., Haghighipour N., Lee C.-U., Scullion E. M., 2012, MNRAS, 420, 3609
Horner J., Wittenmyer R. A., Hinse T. C., Tinney C. G., 2012, MNRAS, 425, 749
Iben I., Jr., Livio M., 1993, PASP, 105, 1373
Kamiński K. Z. et al., 2007, AJ, 134, 1206
Käpylä P. J., 2019, A&A, 631, A122
Käpylä P. J., Mantere M. J., Guerrero G., Brandenburg A., Chatterjee P., 2011, A&A, 531, A162
Käpylä P. J., Mantere M. J., Brandenburg A., 2012, ApJ, 755, L22
Käpylä P. J., Mantere M. J., Cole E., Warnecke J., Brandenburg A., 2013, ApJ, 778, 41
Käpylä M. J., Käpylä P. J., Olspert N., Brandenburg A., Warnecke J., Karak B. B., Pelt J., 2016, A&A, 589, A56
Käpylä P. J., Gent F. A., Olspert N., Käpylä M. J., Brandenburg A., 2019, GAFD, 113, 149
Kupka F., Muthsam H. J., 2017, Liv. Rev. Comp. Astrophys., 3, 1
Lanza A. F., 2005, MNRAS, 364, 238
Lanza A. F., Rodonò M., 1999, A&A, 349, 887
Lanza A. F., Rodonò M., 2004, Astron. Nachr., 325, 393
Lanza A. F., Piluso N., Rodonò M., Messina S., Cutispoto G., 2006, A&A, 455, 595
Marchioni L., Guinan E. F., Engle S. G., Dowling Jones L., Michail J. M., Werner G., Ribas I., 2018, Res. Notes Am. Astron. Soc., 2, 179
Matranga M., Drake J. J., Kashyap V., Steeghs D., 2012, ApJ, 747, 132
Meyer F., Meyer-Hofmeister E., 1979, A&A, 78, 167
Muneer S., Jayakumar K., Rosario M. J., Raveendran A. V., Mekkaden M. V., 2010, A&A, 521, A36
Navarrete F. H., Schleicher D. R. G., Zamponi Fuentealba J., Völschow M., 2018, A&A, 615, A81
Paczynski B., 1976, in Eggleton P., Mitton S., Whelan J., eds, Proc. IAU Symp. 73, Structure and Evolution of Close Binary Systems. Kluwer, Dordrecht, p. 75
Pandey J. C., Singh K. P., 2008, MNRAS, 387, 1627
Parsons S. G., Marsh T. R., Copperwheat C. M., Dhillon V. S., Littlefair S. P., Gänsicke B. T., Hickman R., 2010a, MNRAS, 402, 2591
Parsons S. G. et al., 2010b, MNRAS, 407, 2362
Parsons S. G. et al., 2013, MNRAS, 429, 256
Perdelwitz V. et al., 2018, A&A, 616, A161
Ribeiro T., Kafka S., Baptista R., Tappert C., 2010, AJ, 139, 1106
Rüdiger G., 1989, Differential Rotation and Stellar Convection: Sun and Solar-type Stars. Akademie Verlag, Berlin
Rüdiger G., Elstner D., Lanza A. F., Granzer T., 2002, A&A, 392, 605
Schleicher D. R. G., Dreizler S., 2014, A&A, 563, A61
Schwope A. D., Hambaryan V., Schwarz R., Kanbach G., Gänsicke B. T., 2002, A&A, 392, 541
Taam R. E., Ricker P. M., 2010, New Astron. Rev., 54, 65
Taam R. E., Sandquist E. L., 2000, ARA&A, 38, 113
Vanderbosch Z. P., Clemens J. C., Dunlap B. H., Winget D. E., 2017, in Tremblay P. E., Gaensicke B., Marsh T., eds, ASP Conf. Ser.Vol. 509, 20th European White Dwarf Workshop. Astron. Soc. Pac., San Francisco, p. 571
Viviani M., Warnecke J., Käpylä M. J., Käpylä P. J., Olspert N., Cole-Kodikara E. M., Lehtinen J. J., Brandenburg A., 2018, A&A, 616, A160
Viviani M., Käpylä M. J., Warnecke J., Käpylä P. J., Rheinhardt M., MPS ReSoLVE/Aalto IAG, 2019, preprint (arXiv:1902.04019)
Völschow M., Banerjee R., Hessman F. V., 2014, A&A, 562, A19
Völschow M., Schleicher D. R. G., Perdelwitz V., Banerjee R., 2016, A&A, 587, A34
Völschow M., Schleicher D. R. G., Banerjee R., Schmitt J. H. M. M., 2018, A&A, 620, A42
Warnecke J., Käpylä P. J., Käpylä M. J., Brandenburg A., 2016, A&A, 596, A115
Webbink R. F., 2008, in Milone E. F., Leahy D. A., Hobill D. W., eds, Astrophysics and Space Science Library, 352, Common Envelope Evolution Redux, Springer-Verlag, Berlin. p. 233
Williamson J. H., 1980, J. Comput. Phys., 35, 48
Yadav R. K., Christensen U. R., Wolk S. J., Poppenhaeger K., 2016, ApJ, 833, L28
Zorotovic M., Schreiber M. R., 2013, A&A, 549, A95

This paper has been typeset from a TEX/LATEX file prepared by the author.